POLITECNICO
MILANO 1863

DIPARTIMENTO DI MECCANICA

mecc

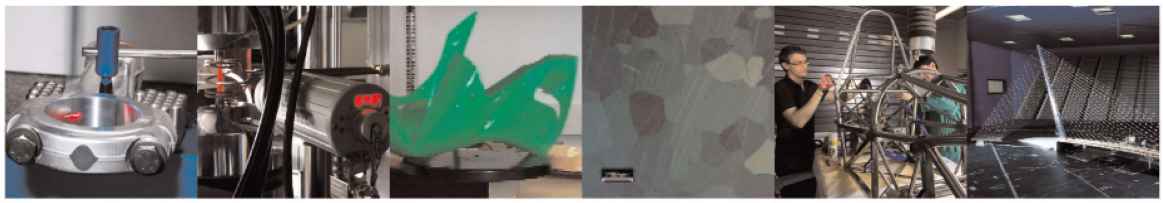

X-ray CT-Based Defect Evaluation of Continuous CFRP Additive Manufacturing

Stefano Petrò, Cesare Reina, Giovanni Moroni

This is a post-peer-review, pre-copyedit version of an article published in Journal of Nondestructive Evaluation. The final authenticated version is available online at: http://dx.doi.org/10.1007/s10921-020-00737-7

DIPARTIMENTO DI MECCANICA ■ POLITECNICO DI MILANO
via G. La Masa, 1 ■ 20156 Milano ■ EMAIL (PEC): pecmecc@cert.polimi.it
http://www.mecc.polimi.it
Rev. 0

Journal of Nondestructive Evaluation manuscript No.
(will be inserted by the editor)

X-ray CT-based defect evaluation of continuous CFRP additive manufacturing

Stefano Petrò · Cesare Reina · Giovanni Moroni

Received: date / Accepted: date

Abstract The spread of additive technologies from prototyping to manufacturing has made the development of new products possible, but still needs effective methods in order to allow their characterization. In particular, porosity is considered a crucial aspect of AM products. A prototype system for the deposition of continuous carbon fiber-reinforced polymers with a thermoplastic matrix has been recently developed, at Mechanical Engineering Department of Politecnico di Milano. This application is of interest, as it would avoid the expensive development and manufacturing of specific molds. The mechanical performance of the manufactured components depends mainly on porosity and on non-correct adhesion among filaments, even in the case of conventional manufacturing processes. The additive deposition shows even more relevant issues of this kind. Hence the need for a characterization of the process. The conventional approach considers a destructive test to characterize the composite mechanical properties or porosity. The aim of this paper is proposing original approaches to evaluate both porosity and non-correct adhesion by means of X-Ray computed tomography. The method is validated by comparing the porosity with the reference destructive method defined in the ASTM D3171 standard. It is also shown that the amount of defects is correlated to the mechanical properties of the obtained components, thus the approach can be used for a non-destructive evaluation of the manufactured parts.

S. Petrò, C. Reina and G. Moroni
Mechanical Engineering Department, Politecnico di Milano,
Via La Masa 1, 20156, Milano, Italy
Tel.: +39-02-2399-8530
E-mail: stefano.petro@polimi.it

Keywords Additive Manufacturing · Inspection · X-Ray Computed Tomography · Continuous Carbon Fiber Reinforced polymers

1 Introduction

The spread of Additive Manufacturing (AM) technologies is reaching applications, which in the past were almost impossible to be considered. If the application of AM to polymeric materials is a standard today, and close to be a standard for metals, its application to composite materials [1] is more difficult, due to the need of managing simultaneously the matrix and the fiber. This is still uncomplicated when dealing with short-fiber reinforced polymers, but more complex for continuous fiber reinforced polymers.

Continuous carbon fiber reinforced polymers (CFRP) are among the most common composites, thanks to their high stiffness/weight ratio. Conventional technologies for manufacturing continuous CFRP include molding, vacuum bagging, compression molding, and filament winding. It is worth noting that these technologies are somehow additive: in fact, they consist in lying carbon fibers and polymer on some mold or mandrel, and then harden the polymer. However, since CFRP are often used in small batch productions, the cost of the mold can limit its diffusion. This justifies the development of additive manufacturing (AM) methods for continuous CFRP [2–6]: by stacking layers of CFRP directly no mold is needed.

As for all new technologies, additive manufacturing continuous carbon fiber reinforced polymers (AMC-CFRP) needs to be characterized. Porosity in particular affects performance. Several attempts have been made to study this behavior and predict the locations of its

occurrence. Gauvin *et al.*[7] analytically linked it to the cavity pressure. Toscano and Vitiello [8] showed how the stacking sequence could yield a higher propensity of the porosity to occur, while Costa *et al.*[9] studied the effect of porosity on moisture absorption and showed how a significant amount of absorption may occur depending on the void content and polymer system.

Standard methods for characterizing composites are based on destructive testing [10, 11]. This approach is usually unsuitable for characterizing AM parts. X-Ray Computed Tomography (XCT) has proven to be a valid non-destructive alternative for the characterization of CFRP. XCT application has shown the possibility of characterizing several properties of CFRP, including porosity [12–16], delamination defects [17–20], and fiber orientation [21]. All the proposed examples consider only CFRP manufactured by conventional technologies, in some cases linking the obtained parameters (porosity in particular) to mechanical properties [22].

However, AMCCFRP differ in their 3D structure from conventional CFRP. In particular, the effect of layers adhesion and delamination is not properly addressed by conventional approaches. Authors discussing application to AMCCFRP include Goh *et al.*[23], Parandoush *et al.*[24], and He *et al.*[25], who all tried to link the porosity to the mechanical properties of the composites. However, these works consider only the internal porosity of the material, neglecting the fact that porosity could open into the external environment.

In this work, an XCT-based method for characterizing voids and defects of AMCCFRP is proposed. The use of XCT for the characterization of porosity is accurately developed in the I&M literature [26–34]; however, its application to AMCCFRP and CCFRP in general is novel.The method is based on the distinction between closed voids, which depict the porosity due to the AM deposition and to the characteristics of the polymer, and open voids, which measure the delamination of the composite. The evaluation of closed voids (porosity) is validated by comparison to the reference destructive methods described in the ASTM D3171 [35] standard. The measured closed void fraction is also compared to the results that can be obtained with the VGSTUDIO MAX 3.4 ® commercial software. Then the correlation between the measure of adhesion defects and flexural mechanic properties (as defined in the ASTM D790 [10] standard) is experimentally shown. The proposed method can nonetheless be helpful to characterize AMCCFRP and for a non-destructive test of products.

2 Experimental setup

An innovative CFRP 3D printing system has been developed at Politecnico di Milano, based on Fused Deposition Modeling (FDM) and Automated Fiber Placement (AFP). The printing head is composed of the feeding system, the heat sink, the hot chamber, the ⌀2 mm nozzle and the compacting system. Temperature, feed-rate and wire tension can be adjusted. The compacting system presses the deposited material with an adjustable force and is needed to guarantee good adhesion between the 3D printed layers. The printing head is mounted on a Fanuc anthropomorphic robot, allowing a large deposition volume.

The feedstock is a ⌀2 mm commingled yarn nominally composed by continuous carbon fibre wires (41% in volume) and Nylon PA12 wires (59% in volume) [36] . The 3D printing process differs from a standard FDM,as only the polymeric fraction of the feedstock is melted. Before deposition, the feedstock is pre-consolidated on a specifically developed pre-consolidation system, which is used to pre-extrude (at an adjustable temperature) the feedstock, making it more rigid.

3 Estimate of the fraction of closed and open voids

Even if the deposition is possible, the CFRP 3D printing system described in §2 has shown severe limitations in the quality of the deposited composite. If the deposition parameters are not close enough to the optimal set-up point, severe delamination and porosity defects are found. This leads to the investigation of an XCT-based characterization of the quality of the deposition.

Suppose that an available sample has been scanned by XCT. Consider as z axis of the sample the direction along which the fibers are deposited. Fig. 1 shows an example of an XCT z-slice of an AMCCFRP sample. Each sample was composed by two layers, each of them was composed by 6 strands of filaments. White regions are representing a slice of each single individual strand of filament, and correspond to the presence of material in the sample. The specimen was printed maintaining each specimen layer parallel to the printing bed. In other words, the first layer, composed of six strands of filament represented in the bottom of the image, was touching the printing bed. The slice clearly shows the presence of porosity in the sample (closed voids, for example highlighted by the red circle). The yellow circles mark areas in which no porosity is present (actually the material is absent), and the fibers do not correctly adhere to each other. This can be related to both an incorrect deposition of the feedstock and to a

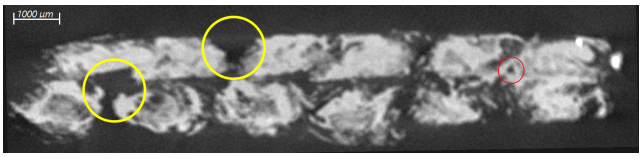

Fig. 1 Example of XCT slice of an AMCCFRP sample. The yellow circles indicate "open voids"; the red circle indicates a "closed void".White and grey areas of the image represents the parts of the samples where there is a prensece of material.

successive delamination of the composite due to residual strains. We call these areas "open voids", as they are connected to the exterior of the part. Conventional porosity evaluation would fail in identifying these defects: their connection to the exterior of the part makes them different from conventional porosity. As they are expected to affect the resistance of the sample, a non-destructive way of automatically quantifying them is needed.

Open voids are expected to be related to deposition issues, so their estimate is relevant for the characterization of the part functionality. The proposed method analyses the XCT image (voxel representation) to estimate the fraction of open and closed voids in the sample. The approach is constituted essentially by four steps: binarization, outlier removal, identification of the mask, and identification of the open and closed voids. Although a voxel representation is being analyzed, considering it in its three-dimensional nature is difficult and requires significant computational power. To reduce the computational power required and to make the method applicable even when the XCT images are large, the XCT image itself will be analyzed slice by slice. In particular, the first three steps consider the slices singularly, while the fourth compares the various slices of the image.

3.1 Binarization

Binarization converts the original grayscale image into black and white. This is made possible by the identification of a threshold for the grey-values (GV): voxels characterized by a GV higher than the threshold are set to white and the remaining ones to black. Several methods can be found in literature for the identification of the threshold. In this work we considered the most diffused methods, namely Otsu's method [37] and the ISO50 method [38]. The results from these two methods will be compared in §4 and §5.

The threshold should be selected slice by slice rather than globally because experience has shown that, due to limitations in XCT, the contrast and overall intensity can vary significantly from the upper to the lower part of the sample. A global threshold could lead to an incorrect binarization.

3.2 Outlier removal

It has been observed that, due to adhesion problems, often samples created with the CFRP 3D printing system present single carbon fibers that are not connected to the rest of the sample. As they are not connected to the rest of the part, these fibers do not contribute significantly to the global resistance of the sample. However, since they are recognized as made of material during the binarization, they could influence the identification of the mask described in §3.3, and later the estimate of the voids. Furthermore, often artifacts in XCT images look like circle arcs or isolated voxels outside the sample. Since they are recognized as materials even during the binarization, they could similarly affect the mask and the estimate of the open voids. Therefore, "outliers" must be removed.

The removal of outliers is simply based on the area they occupy in the single slide. The cross-section of the feedstock filament used in our case study, which is ⌀2 mm, is equal to 3.14 mm^2. All isolated blobs of voxels in the binarized area, i.e., all the groups of voxels above the threshold that are completely surrounded by voxels below the threshold, have to be identified. It is proposed that any blob of voxels in the binarized image characterized by an area smaller than 5% of the feedstock filament cross-section (0.2 mm^2 in our case) is considered an outlier and eliminated, as shown in Fig. 2. As each voxel occupies the same volume (or area in a single slice), this value can be easily converted into the number of voxels (2500 in our case study) in a slice of the voxel representation.

3.3 Identification of the mask

Once the outliers have been removed, the region of interest (ROI) can be identified. The region of interest will exclude only voxels above the threshold in the binarized image. To be able to estimate the void fraction, also the void area must be included.

The definition of ROI is similar to the identification of the convex hull of the part. The convex hull [39] contains all the material and excludes the void surrounding the part. The convex hull is well defined on (2D and 3D) clouds of points, however not on images. Therefore, first an iso-profile is defined on the binarized image with the outliers removed. The iso-profile is a set of points located at the transition from material to air, as identified by the threshold.

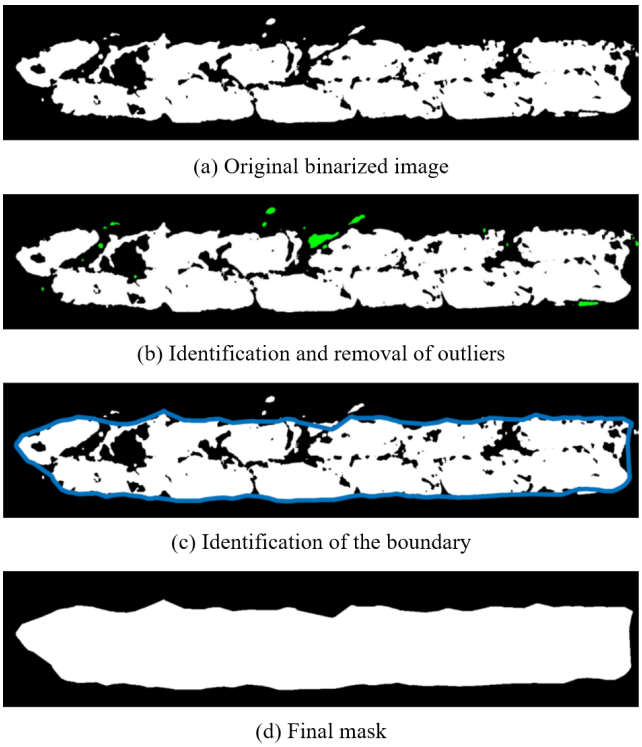

(a) Original binarized image

(b) Identification and removal of outliers

(c) Identification of the boundary

(d) Final mask

Fig. 2 Outliers identification and removal, and definition of the mask.

However, the results that are produced in §5 have indicated that the convex hull is not a good choice when evaluating the void fraction. Consider for instance that, if the binarized slice is banana-shaped, the convex hull would include the concavity, which is completely external. Therefore, a boundary is defined by using the "boundary.m" function implemented in Matlab® rather than applying the classic convex hull. This function, given a set of points, identifies a sub-set of points defining a non-convex polygon containing all points. The generated polygon follows closely the points of the iso-profile, but it will not include all points of the iso-profile. Of course, it will not include points corresponding to an internal void. Regarding the other points, its behavior can be tuned by defining a shrink factor. A high shrink factor value leads to a boundary that includes all possible points. Lower values generate a polygon more similar to the convex hull. The choice will be discussed in §5. Comparing the boundary to the convex hull (Fig. 3), it is evident that in this way it is possible to have a better identification of the limit between the sample and the surrounding air.

The portion of binarized image inside the polygon defines the mask, i.e. the zone of the slice that will be considered for the calculation of the open and closed void fraction.

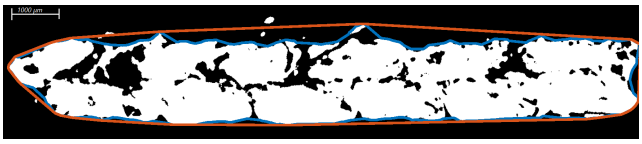

Fig. 3 Comparison between convex hull (red) and boundary polygon (blue). Please note the outliers are not considered in the definition of the hull/polygon.

Once the mask has been defined for every slice, it is possible to calculate the total fraction of void as

$$VF = \frac{\sum_{i=1}^{N} NB_i}{\sum_{i=1}^{N} NT_i} \tag{1}$$

where N is the number of slices, and NT_i and NB_i are respectively the total number of voxels and the number of black voxels (under the threshold) inside the mask of the i^{th} slice.

3.4 Identification of the closed voids

The VF defined in (1) does not distinguish voids connected to the outside (open voids), which are related to adhesion defects, and fully internal defects (closed voids), which constitute the porosity. As it is uncertain whether both open and closed voids influence the composite resistance, a method to distinguish them is required.

A procedure that distinguishes the two is described in the following steps (Fig. 4).

1. Sort the slices according to their z level. Set $i = 1$.
2. Start from the bottom slice (slice 1), and identify all closed voids in this slice. A void is a continuous group of voxels whose GV is lower than the threshold defined in §3.1. A void is considered closed if none of its voxels belong to the edge of the mask defined in 3.3, otherwise it is considered open.
3. Increase i by 1.
4. Identify all open and closed voids in slice i as explained in point 2.
5. Consider closed voids in slice i. If any voxel in a closed void corresponds to a voxel of slice $i-1$ belonging to an open void, then the closed void is redefined as open void (Fig. 5)
6. Keep iterating on point 3 until the last slice N is reached.
7. Decrease i by 1.
8. A (tentative) identification of open and closed voids in slice i is already available.
9. Consider closed voids in slice i. If any voxel in a closed void corresponds to a voxel of slice $i+1$ be-

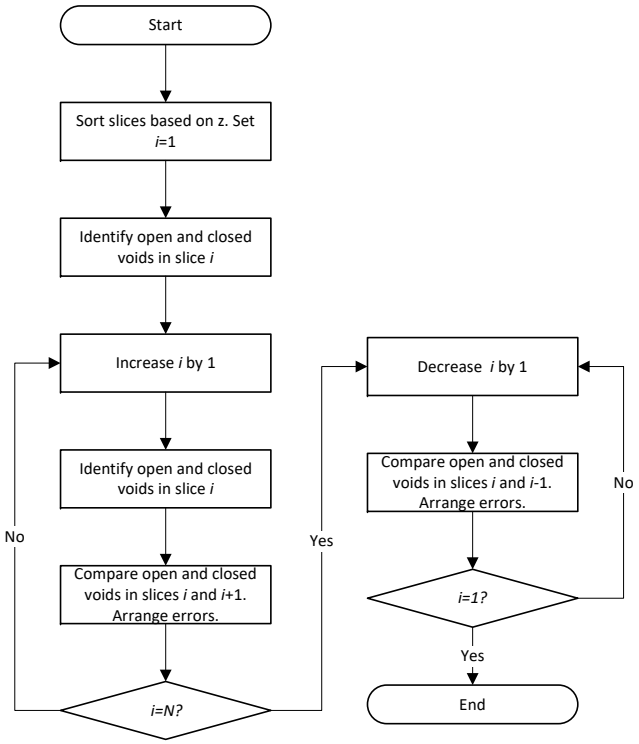

Fig. 4 Flux diagram for the identification of open and closed voids.

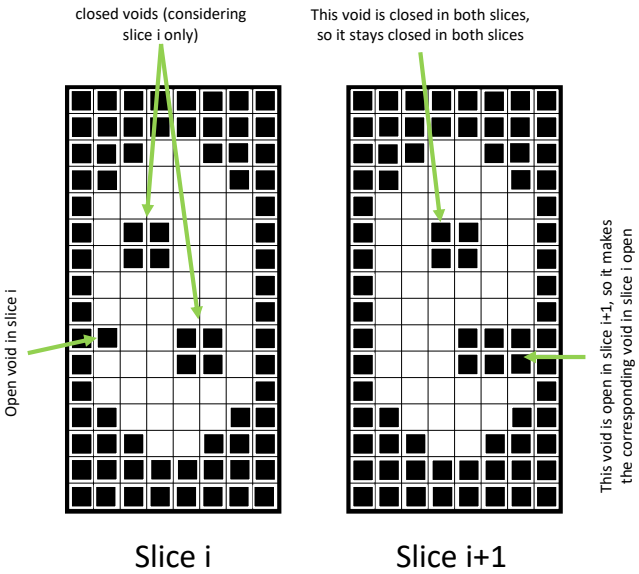

Fig. 5 Identification of the open/closed voids: an open void over a closed void makes the closed void open.

longing to an open void, then the closed void is redefined as open void.

10. Keep iterating on point 7 until slice 1 is reached.

Now the fractions of open and closed voids are respectively estimated as:

$$VFC = \frac{\sum_{i=1}^{N} NBC_i}{\sum_{i=1}^{N} NT_i} \tag{2}$$

$$VFO = \frac{\sum_{i=1}^{N} NBO_i}{\sum_{i=1}^{N} NT_i} \tag{3}$$

where NBC_i, NBO_i are the number of voxels belonging respectively to closed and open voids in the i^{th} slice.

4 Validation – porosity measurement

The standard way of evaluating porosity [35] is a destructive test. The test measures the relative content of air inside the sample. As such, it cannot measure the fraction of open voids, which is not entirely inside the sample. Therefore, it will be applied to the calculated VFC value only.

A set of eight 35x12x2 mm two-layered AMCCFRP samples has been prepared and tested by applying the matrix carbonization into a nitrogen-purging furnace test described in ASTM D3171-15. All samples have been manufactured under the same condition, that is:

- Feed rate: 3 mm/s
- Consolidation Temperature: 305°C
- Extrusion Temperature: 305°C
- Compacting force: 25 N

The samples were then scanned on a NSI X25 XCT scanner considering the following scan parameters:

- Source voltage: 30 KV
- Source intensity: 300 µA
- Integration time: 75.54 ms
- Voxel size: 9.5 µm
- Angle step: 0.18°
- Frame Averaging: 10 averaged frames
- No physical filter
- Binning: 1x1
- Source to detector distance: 246.3 mm
- Source to sample distance: 30.9 mm

With reference to the image processing parameters, neither image binning nor image filtering has been used. The method has been applied directly on the original raw images. Supposing that, in order to visually detect a pore, its size must be approximately equal to at least 3 voxels, one may expect 30 µm pores to be identifiable in the images.

The fraction of closed voids was then estimated via both the ASTM D3171-15 standard method and the algorithm described in §3. Fig. 6 and Fig. 7 compare

the values obtained with the destructive test and the XCT estimate when the Otsu's and ISO50 thresholds are applied respectively. Excluding an anomalous value, a strong correlation is visible. From a statistical point of view, with the Otsu's threshold, the Pearson's correlation coefficient is, in fact, equal to 0.78, and is statistically significant. Going more in-depth, the regression equation is $VFC = -0.54 + 0.95VCF_e$, where VCF_e is the value of VCF measured according to the standard procedure. The regression constant is not statistically significant, so there is no systematic difference between the porosity value indicated by the two methods. The regression coefficient does not differ statistically from 1. Furthermore, the residual error has a standard deviation equal to 0.7%. The results that can be obtained with the ISO50 threshold are substantially identical: the (significant) Pearson's correlation coefficient is equal to 0.80, the regression equation is $VFC = -1.08 + 1.01VCF_e$. Again, the regression constant is not statistically significant, the regression coefficient does not differ statistically from 1, and the residual error has a standard deviation equal to 0.7%. Therefore, we can assume our method is adequately accurate.

The estimated VCF has been compared to the void fraction value that can be obtained applying the VGSTUDIO MAX 3.4 ® commercial software to the XCT images. The "porosity analysis (VGDefX)" module was considered. Material definition was based on the determined surface. The porosity calculation used an area size of a single voxel. No filter was applied on the results. In this case, however, no statistically significant correlation can be found between the VGSTUDIO MAX estimates and our method. In addition, VGSTUDIO MAX estimates are not correlated to the ASTM D3171-15 reference porosity measurements. There is a (statistically significant) 3.4% average difference between standard and VGSTUDIO MAX measurement results. It is possible to conclude that VGSTUDIO MAX estimates of the porosity are not consistent with the reference destructive method.

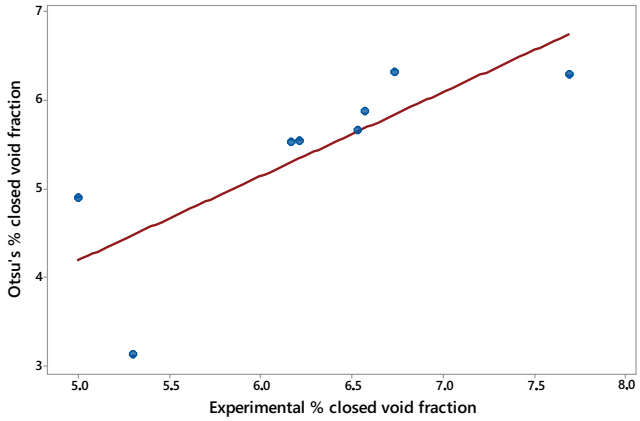

Fig. 6 Correlation between destructive and XCT estimate of the porosity – Otsu's threshold.

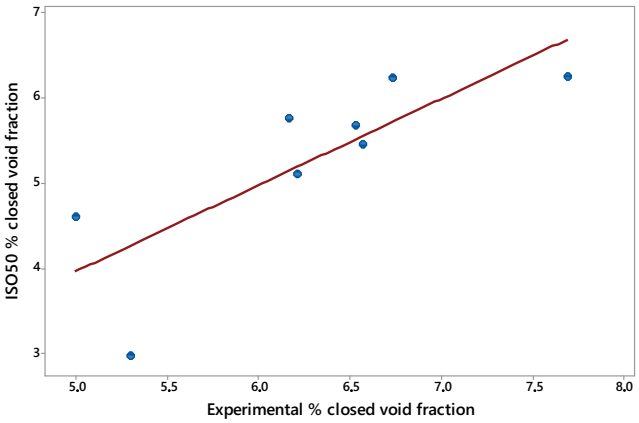

Fig. 7 Correlation between destructive and XCT estimate of the porosity – ISO50 threshold.

Table 1 Parameters for the factorial experiment.

	FACTOR LEVEL	
Design factor	LOW	HIGH
Extrusion consolidation temperature °C	275	305
Feed rate [mm/s]	3	10
Wire tension [N]	1.2	3
Extrusion temperature °C	275	305
Compacting force [N]	0	25
Distance of load cells from nozzle [mm]	21.64	25

5 Correlation with flexural strength

To prove the effectiveness of the void fraction as a parameter to forecast the integrity of parts, experimentation has been conducted developing a 2^{6-1} (total of 32 samples) factorial experiment. The use of a factorial design guarantees that the values obtained for the void fraction and the flexural strength will cover most of the possible values. The values of the parameters were chosen based on the operators' experience, so that they are the maximum/minimum acceptable. This might lead to conditions in which parts cannot be manufactured. The values considered for the various factors in the experiment are reported in Tab. 1.

The 75x12x2 mm two-layered AMCCFRP samples were prepared according to the ASTM D790-17 [10] standard. All samples were scanned on the same XCT scanner and with the same acquisition parameters described in §4. Then their flexural strength was measured by running a three-point-bending test according to ASTM D790-17. In particular, the rate of crosshead motion, R [mm/mm/min], has been computed according to the following equation

$$R = \frac{ZL^2}{6d} \tag{4}$$

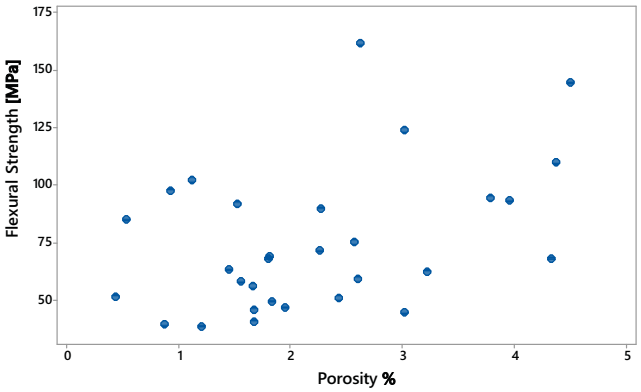

Fig. 8 Correlation between flexural strength and closed porosity - Otsu's method

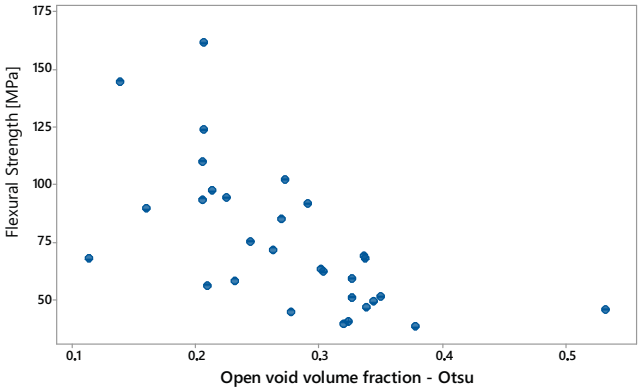

Fig. 9 Correlation between flexural strength and open porosity – Otsu's threshold – optimal shrink factor.

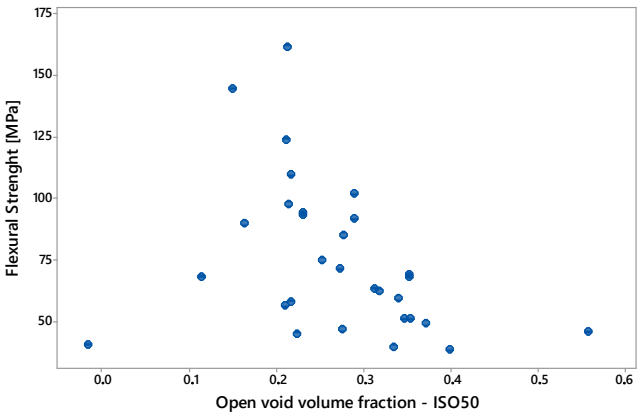

Fig. 10 Correlation between flexural strength and open porosity – ISO50 threshold – optimal shrink factor.

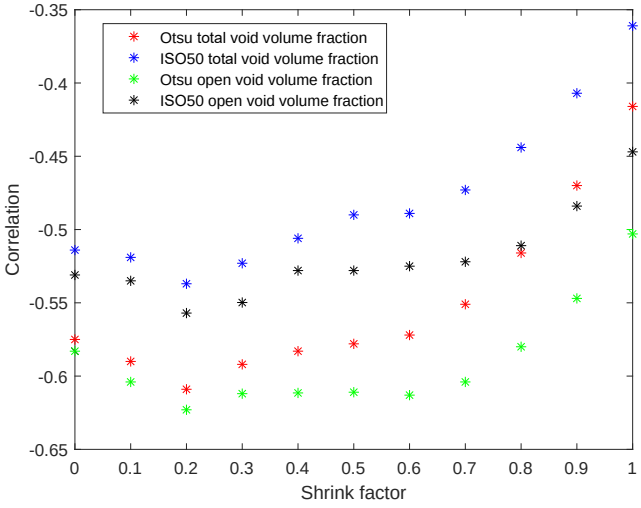

Fig. 11 Choice of the optimal shrink factor.

where L is the support span (60 mm in the test), d is the depth of beam (1.8 mm), and Z the rate of straining of the outer fiber (120 mm/min).

Fig. 8 shows a scatter-plot of the closed porosity fraction versus the flexural strength. No particular trend or correlation is apparent. A statistical analysis indicates that there is only a weak yet significant correlation. This scarce correlation indicates that closed porosity is not a good indicator of the quality of the part from a mechanical point of view, if non-correct adhesion is present and relevant: the impact of porosity on the part performance is marginal.

On the other hand, Fig. 9 and 10 show the correlation between open voids and flexural strength for the Otsu's and ISO50 thresholds respectively. In this case, the correlation is apparent, and the flexural strength appears to be inversely proportional to the open void fraction. It is also apparent that the two considered thresholds yield similar results.

As mentioned in §3.3, in order to apply the "boundary" function the definition of a shrink factor is needed. The shrink factor ranges from 0 to 1, and affects how closely the boundary follows the points. The value zero corresponds to the convex hull of the points, and increasing values generate boundaries more and more "tailored" to the points. To select the optimal value, the Pearson's correlation coefficient between the flexural strength and the open void fraction has been calculated for different values of the shrink factor itself. Fig. 11 shows that the maximum (negative, the absolute value is considered) correlation is found when the shrink factor is equal to 0.2. The corresponding values of the Pearson's correlation coefficient are respectively equal to -0.623 for Otsu's and -0.557 for the ISO50 thresholding and are statically significant. This, together with Fig. 11, indicates that Otsu's threshold slightly outperforms the ISO50 threshold. Fig. 11 also shows the correlation coefficient between the flexural strength and the total void fraction. The open void fraction outperforms it in terms of correlation with the flexural strength. This is due to the removal of the closed void fraction from the total voids. Porosity (closed voids) actually acts as a sort of noise on the correlation.

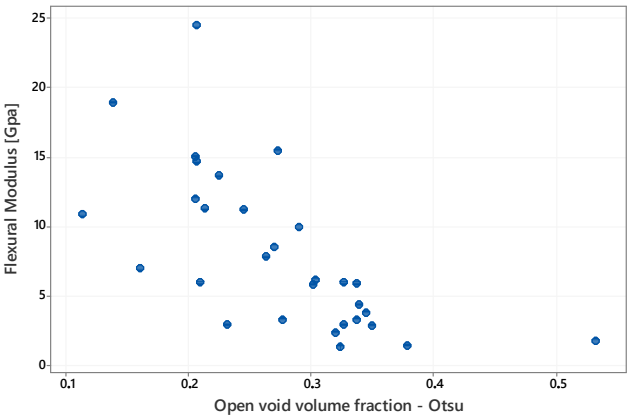

Fig. 12 Correlation between flexural modulus and open porosity – Otsu's threshold – optimal shrink factor.

Having identified the optimal threshold (Otsu's) and shrink factor (0.2), it is also possible to investigate the correlation between the flexural modulus and the porosity. The correlation between the VF and the flexural modulus is significant and equal to -0.632. The correlation between the VFO and the flexural modulus (Fig. 12) is significant as well and similar in value, -0.657. It is worth noting that this value is similar to the one obtained for the correlation with the flexural strength.

The open void fraction is then expected to adequately describe the quality of the deposition obtained. It appropriately measures whether the filament was correctly deposited or not.

6 Conclusions

The spread of additive technologies from prototyping to manufacturing has made the development of new products possible, but still needs effective methods in order to allow their characterization. In particular, porosity is considered a crucial aspect of AM products.

A prototype system for the deposition of commingled yarns of nylon and carbon fiber has been developed, but characterization is still needed. Conventional characterization includes the use of destructive methods for evaluating both porosity and mechanical properties. Destructive testing is unfeasible on final parts and more in general when small batches are considered.

To make non-destructive testing possible, XCT has been considered in order to investigate the structural characteristics of the products. A method to evaluate the closed (not connected to the outside) and open (connected to the outside) void fraction from an XCT image of the part has been developed. The latter has shown to be strongly correlated to the mechanical properties of the parts. This correlation is explained by the open void fraction describing the good or not good adhesion of filaments. It can then be considered an effective parameter for non-destructive testing of parts.

Future developments include the study of the shape of open and closed voids to better link them to flexural characteristics of parts, and the use of artificial intelligence techniques to choose the shrink factor to be applied, making its choice automatic. Besides, in the current version, a constant shrink factor was applied to all slices. The possibility of considering different slice-by-slice values will be considered.

Acknowledgment

We gratefully acknowledge the Italian Ministry of Education, University and Research for the support provided throughout the Project "Department of Excellence LIS4.0 - Lightweight and Smart Structures for Industry 4.0" (CUP: D56C18000400006).

References

1. Goh GD, Yap YL, Agarwala S, Yeong WY (2019) Recent Progress in Additive Manufacturing of Fiber Reinforced Polymer Composite. Advanced Materials Technologies 4(1):1800271, DOI 10.1002/admt.201800271
2. Matsuzaki R, Ueda M, Namiki M, Jeong TK, Asahara H, Horiguchi K, Nakamura T, Todoroki A, Hirano Y (2016) Three-dimensional printing of continuous-fiber composites by in-nozzle impregnation. Scientific Reports 6:23058, DOI 10.1038/srep23058
3. Li N, Li Y, Liu S (2016) Rapid prototyping of continuous carbon fiber reinforced polylactic acid composites by 3D printing. Journal of Materials Processing Technology 238:218–225, DOI 10.1016/j.jmatprotec.2016.07.025
4. Yang C, Tian X, Liu T, Cao Y, Li D (2017) 3D printing for continuous fiber reinforced thermoplastic composites: Mechanism and performance. Rapid Prototyping Journal 23(1):209–215, DOI 10.1108/RPJ-08-2015-0098
5. Blok LG, Longana ML, Yu H, Woods BK (2018) An investigation into 3D printing of fibre reinforced thermoplastic composites. Additive Manufacturing 22:176–186, DOI 10.1016/j.addma.2018.04.039
6. van de Werken N, Tekinalp H, Khanbolouki P, Ozcan S, Williams A, Tehrani M (2020) Additively manufactured carbon fiber-reinforced composites: State of the art and perspective. Additive Man-

ufacturing 31:100962, DOI 10.1016/j.addma.2019.100962
7. Gauvin R, Chibani M, Lafontaine P (1987) The Modeling of Pressure Distribution in Resin Transfer Molding. Journal of Reinforced Plastics and Composites 6(4):367–377, DOI 10.1177/073168448700600406
8. Toscano C, Vitiello C (2011) Influence of the stacking sequence on the porosity in carbon fiber composites. Journal of Applied Polymer Science 122(6):3583–3589, DOI 10.1002/app.34769
9. Costa ML, Rezende MC, de Almeida SFM (2006) Effect of void content on the moisture absorption in polymeric composites. Polymer - Plastics Technology and Engineering 45(6):691–698, DOI 10.1080/03602550600609549
10. American Society for Testing and Materials International (2017) ASTM D790-17: Standard Test Methods for Flexural Properties of Unreinforced and Reinforced Plastics and Electrical Insulating Materials. DOI 10.1520/D0790-17
11. Hao W, Liu Y, Zhou H, Chen H, Fang D (2018) Preparation and characterization of 3D printed continuous carbon fiber reinforced thermosetting composites. Polymer Testing 65:29–34, DOI 10.1016/j.polymertesting.2017.11.004
12. Kastner J, Plank B, Salaberger D, Sekelja J (2010) Defect and Porosity Determination of Fibre Reinforced Polymers by X-ray Computed Tomography. In: NDT in Aerospace 2010 - We.1.A.2, pp 1–12
13. Liu X, Chen F (2016) Defects Characterization in CFRP Using X-ray Computed Tomography. Polymers and Polymer Composites 24(2):149–154, DOI 10.1177/096739111602400210
14. Stamopoulos AG, Tserpes KI, Dentsoras AJ (2018) Quality assessment of porous CFRP specimens using X-ray Computed Tomography data and Artificial Neural Networks. Composite Structures 192:327–335, DOI 10.1016/j.compstruct.2018.02.096
15. Mehdikhani M, Nguyen NQ, Straumit I, Gorbatikh L, Lomov SV (2018) Analysis of void morphology in composite laminates using micro-computed tomography. In: IOP Conference Series: Materials Science and Engineering, Institute of Physics Publishing, vol 406, DOI 10.1088/1757-899X/406/1/012010
16. Nguyen NQ, Mehdikhani M, Straumit I, Gorbatikh L, Lessard L, Lomov SV (2018) Micro-CT measurement of fibre misalignment: Application to carbon/epoxy laminates manufactured in autoclave and by vacuum assisted resin transfer moulding. Composites Part A: Applied Science and Manufacturing 104:14–23, DOI 10.1016/j.compositesa.2017.10.018
17. Wright P, Fu X, Sinclair I, Spearing S (2008) Ultra High Resolution Computed Tomography of Damage in Notched Carbon Fiber—Epoxy Composites. Journal of Composite Materials 42(19):1993–2002, DOI 10.1177/0021998308092211
18. Wright P, Moffat A, Sinclair I, Spearing SM (2010) High resolution tomographic imaging and modelling of notch tip damage in a laminated composite. Composites Science and Technology 70(10):1444–1452, DOI 10.1016/j.compscitech.2010.04.012
19. Scott AE, Mavrogordato M, Wright P, Sinclair I, Spearing SM (2011) In situ fibre fracture measurement in carbon-epoxy laminates using high resolution computed tomography. Composites Science and Technology 71(12):1471–1477, DOI 10.1016/j.compscitech.2011.06.004
20. Sket F, Seltzer R, Molina-Aldareguía JM, Gonzalez C, Llorca J (2012) Determination of damage micromechanisms and fracture resistance of glass fiber/epoxy cross-ply laminate by means of X-ray computed microtomography. Composites Science and Technology 72(2):350–359, DOI 10.1016/j.compscitech.2011.11.025
21. Pinter P, Dietrich S, Bertram B, Kehrer L, Elsner P, Weidenmann KA (2018) Comparison and error estimation of 3D fibre orientation analysis of computed tomography image data for fibre reinforced composites. NDT and E International 95:26–35, DOI 10.1016/j.ndteint.2018.01.001
22. Tserpes KI, Stamopoulos AG (2016) A multi-scale numerical methodology for predicting the mechanical properties of porous CFRP laminates using data from X-ray computerized tomography. In: ECCM 2016 - Proceeding of the 17th European Conference on Composite Materials, pp 1–8
23. Goh GD, Dikshit V, Nagalingam AP, Goh GL, Agarwala S, Sing SL, Wei J, Yeong WY (2018) Characterization of mechanical properties and fracture mode of additively manufactured carbon fiber and glass fiber reinforced thermoplastics. Materials and Design 137:79–89, DOI 10.1016/j.matdes.2017.10.021
24. Parandoush P, Zhou C, Lin D (2019) 3D Printing of Ultrahigh Strength Continuous Carbon Fiber Composites. Advanced Engineering Materials 21(2):1800622, DOI 10.1002/adem.201800622
25. He Q, Wang H, Fu K, Ye L (2020) 3D printed continuous CF/PA6 composites: Effect of microscopic voids on mechanical performance. Composites Science and Technology 191:108077, DOI 10.1016/j.compscitech.2020.108077

26. More N, Basse-Cathalinat B, Baquey C, Lacroix F, Ducassou D (1983) Application of novel techniques of medical imaging to the non-destructive analysis of carbon-carbon composite materials. Nuclear Instruments and Methods In Physics Research 214(2-3):531–536, DOI 10.1016/0167-5087(83)90628-2
27. Kerckhofs G, Schrooten J, Van Cleynenbreugel T, Lomov SV, Wevers M (2008) Validation of x-ray microfocus computed tomography as an imaging tool for porous structures. Review of Scientific Instruments 79(1):013711, DOI 10.1063/1.2838584
28. Yang YS, Gureyev TE, Tulloh A, Clennell MB, Pervukhina M (2010) Feasibility of a data-constrained prediction of hydrocarbon reservoir sandstone microstructures. Measurement Science and Technology 21(4):047001, DOI 10.1088/0957-0233/21/4/047001
29. Bloom M, Russell MJ, Kustau A, Mandayam S, Sukumaran B (2010) Measurement of porosity in granular particle distributions using adaptive thresholding. In: IEEE Transactions on Instrumentation and Measurement, vol 59, pp 1192–1199, DOI 10.1109/TIM.2010.2040902
30. Jin Y, Konno Y, Nagao J (2014) Pressurized subsampling system for pressured gas-hydrate-bearing sediment: Microscale imaging using X-ray computed tomography. Review of Scientific Instruments 85(9):094502, DOI 10.1063/1.4896354
31. Thompson A, Maskery I, Leach RK (2016) X-ray computed tomography for additive manufacturing: a review. Measurement Science and Technology 27(7):72001, DOI 10.1088/0957-0233/27/7/072001
32. Zou C, Marrow TJ, Reinhard C, Li B, Zhang C, Wang S (2016) Porosity characterization of fiber-reinforced ceramic matrix composite using synchrotron X-ray computed tomography. In: Journal of Instrumentation, Institute of Physics Publishing, vol 11, p C03052, DOI 10.1088/1748-0221/11/03/C03052
33. Xu F, Xiao Y, Hu X, Dong B, Liu W, Li Y (2016) In situ investigation of Al-Ti mixed metal system microwave sintering by synchrotron radiation computed tomography. In: Journal of Instrumentation, Institute of Physics Publishing, vol 11, p C02074, DOI 10.1088/1748-0221/11/02/C02074
34. Wang YD, Liu KY, Yang YS, Ren YQ, Hu T, Deng B, Xiao TQ (2016) Quantitative multi-scale analysis of mineral distributions and fractal pore structures for a heterogeneous Junger Basin shale. Journal of Instrumentation 11(4):C04005, DOI 10.1088/1748-0221/11/04/C04005
35. American Society for Testing and Materials International (2015) ASTM D3171-15: Standard Test Methods for Constituent Content of Composite Materials. DOI 10.1520/D3171-15
36. (2020) Concordia Fibers. URL `https://www.concordiafibers.com/index.html`
37. Otsu N (1979) A Threshold Selection Method from Gray-Level Histograms. IEEE Transactions on Systems, Man, and Cybernetics 9(1):62–66, DOI 10.1109/TSMC.1979.4310076
38. International Organization for Standardization (2017) ISO 15708-3: Non-destructive testing - Radiation methods for computed tomography Part 3: Operation and interpretation
39. Rockafellar RT (1970) Convex analysis. Princeton Mathematical Series, No. 28, Princeton University Press, Princeton, N.J.